Polymer Testing 93 (2021) 106965

Contents lists available at ScienceDirect

Polymer Testing

journal homepage: http://www.elsevier.com/locate/polytest

Experimental multi-scale approach to determine the local mechanical properties of foam base material in polyisocyanurate metal panels

P. Gahlen [a,*], S. Fröbel [a], A. Karbach [b], D. Gabriel [b], M. Stommel [c]

[a] Covestro Deutschland AG, Kaiser-Wilhelm-Allee 60, 51373, Leverkusen, Germany
[b] Currenta GmbH & Co. OHG, Kaiser-Wilhelm-Allee 50, 51373, Leverkusen, Germany
[c] Leibniz-Institut für Polymerforschung Dresden e.V. (IPF), Hohe Straße 6, 01069, Dresden, Germany

ARTICLE INFO

Keywords:
Experimental micromechanics
Nanoindentation
Atomic force microscopy
Polyisocyanurate foam

ABSTRACT

Polyisocyanurate (PIR) foams were examined regarding their local chemical composition using ATR-IR spectroscopy. As a special parameter the PIR: Amide III intensity ratio is to be mentioned, which represents the quantity of the formed PIR groups. Based on the local PIR: Amide III intensity ratio, the mechanical properties (Young's modulus) of the foam base material were analyzed at defined positions by AFM and Nanoindentation. It turned out that the AFM method is only suitable for qualitative analysis, because the values differ strongly from macroscopic measurements. For the measurements using nanoindentation, a new embedding method was developed, which achieves significantly more realistic and reproducible results compared to the embedding method used in the literature and shows a very good agreement with the macroscopic values. In general, it has been shown that a higher PIR: Amide III intensity ratio tends to lead to a higher Young's modulus. Nevertheless, there are other, currently unknown characteristic values which also influence the Young's modulus.

1. Introduction

Polyisocyanurate-based metal-foam composite elements, so-called metal panels, are used increasingly for efficient thermal insulation in the construction industry due to their very good flame-retardancy, self-supporting properties combined with low weight and low-cost assembly options [1,2].

The composite elements consist of two flat, lined, or profiled external metallic cover layers of low thickness, usually made of steel sheets, in which the interspace (core layer) is filled with a thermally insulating low-density layer of polyisocyanurate (PIR) rigid foam [3–5]. PIR foams typically contain a mixture of polyurethane (PUR) and PIR groups. The urethanes are typically formed by the addition of polyfunctional isocyanates to active hydrogen groups carrying molecules like multifunctional alcohols. The linear connections (Fig. 1a) of the urethanes render the material flexible and ductile [6]. Isocyanurates can be formed either by a trimerization of isocyanates with the aid of catalysts like carboxylic acid salts or by a stepwise reaction between alcohol and excess isocyanate [6]. In the latter case, carbamate is formed first from alcohol and isocyanate. The carbamate then reacts further with isocyanate to form allophanate and finally isocyanurate. In general, these two reaction paths take place at higher temperatures (min. 60 °C) and form stable, highly branched, ring structures (Fig. 1b) that provide modified mechanical, chemical, and thermal properties compared to those of polyurethanes [6,7]. In addition to an increase in hardness, the PIR structures lead in particular to increased flame retardancy, which is essential in the construction industry. From a technical and economic point of view, the additional reaction of PIR is advantageous compared to additional flame retardants [8].

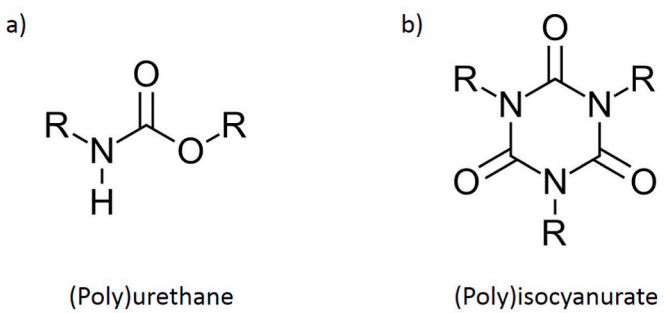

Fig. 1. Scheme of (a) urethane and (b) isocyanurate groups [6,7].

* Corresponding author.
E-mail address: patrick.gahlen@covestro.com (P. Gahlen).

https://doi.org/10.1016/j.polymertesting.2020.106965
Received 5 October 2020; Accepted 15 November 2020
Available online 24 November 2020

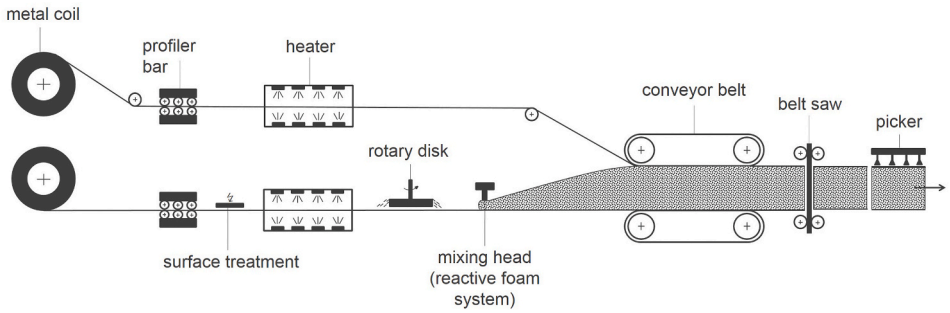

Fig. 2. Schematic continuous production process of metal panels on a DCB. In the beginning, the thin cover layers are fed into the system and profiled. Then the surface of the lower cover layer is physically cleaned and activated by means of surface treatment, usually corona treatment, to achieve a better adhesion. Afterwards, the cover layers are preheated and a polyurethane-based adhesion promoter is applied to the lower cover layer using a rotary disk to further improve the adhesion properties. In the next step, the liquid foam mixture is applied and expands to the upper cover layer. After cooling, the composite element is cut to size and stored.

The metal panels are usually produced continuously on a double conveyor belt (DCB). The production process is shown schematically in Fig. 2. In the continuous production of metal panels, process-related inhomogeneities in the foam occur, which can influence the mechanical properties. The exothermic reactions and self-insulating properties of the foam lead to high temperatures of up to 150 °C in the core of the elements. The conveyor belts are typically preheated to around 60 °C, i. a. to provide sufficient thermal energy to start the reactions. However, at later stages of the reactions, this rather leads to a cooling effect so that reaction heat is dissipated close to the sheets [9]. This leads to a temperature gradient during the production of the part, which finally results in varying chemical compositions of the base material over the element thickness. Due to this effect, the PIR content is larger in the core than close to the metal sheets. Additionally, the cell structures vary along the element thickness due to the temperature gradient and foam flow processes. Changing the belt temperature drastically would not solve these issues and rather lead to adhesion and/or foam collapse issues [9,10].

These effects cause variations of the mechanical and morphological foam properties, which influence the mechanical properties of the metal panels and can lead to premature failure. For this reason, understanding the individual effects is essential for the design of these elements. Experimental observation of the influencing factors is only possible to a limited extent, since these factors always overlap and cannot be analyzed separately. Therefore, mesomechanical finite element modeling is often used, which allows analysis of individual influencing factors [4,11–16].

For an exact numerical design of a mesomechanical foam structure, knowledge of the local foam properties (foam base material, cell size distribution, cell orientation, etc.) is necessary. While the analysis of the cell structure (size and orientation) by means of digital image processing (2D microscopy images or 3D X-ray computed tomography) is already established and has been reported many times in the literature [4,13,17,18], the measurement of the mechanical properties of the foam base material, especially of reactive materials, is still a big challenge.

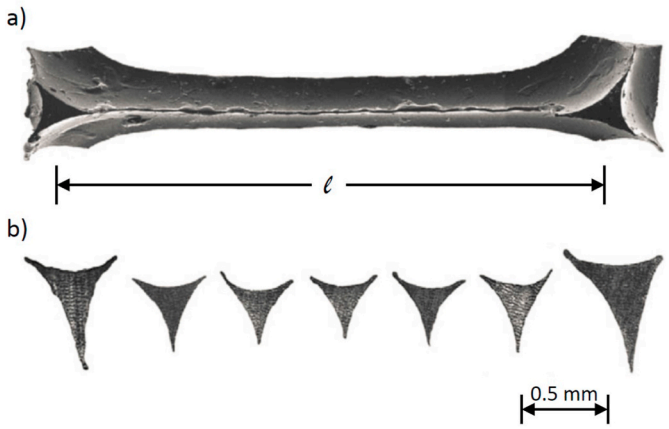

Fig. 3. (a) A typical foam strut and (b) cross-section along its length [23].

In general, two approaches are used to measure the mechanical properties of the foam base material:

1. Indirect measurement using macroscopic measuring methods on a compact material, which is made from the foam system [19–22].
2. Direct measurement on the foam using micro- or nano-scale methods (Micro tensile and bending test, nanoindentation, atomic force microscopy) [11,13,23–25].

Both approaches have advantages and disadvantages. The indirect measurement methods are standardized and thus much easier to perform. However, effects of the processing history (stretching during foaming process and chemical changes by adding foaming agents) cannot be taken into account, although they can have a massive influence on the properties [26,27]. In addition, macro-scale measurements can deviate significantly from micro-scale measurements.

Compared to the indirect measurement methods, the direct methods allow the measurement of the "actual" material, including the processing history. However, microscale methods are much more complex and susceptible to errors. Especially the accuracy of the microscale tensile and bending tests results is not high, because there are many factors that induce error. For example, the non-uniformity and three-cusp hypocycloid shape of the cell strut cross-section (Fig. 3) make it difficult to calculate the mechanical stress. Even small initial curvature and specimen's alignment introduce bending moment, and slip at clamping points leads to overestimated strains [23,25].

Therefore "penetrating" methods (e.g. nanoindentation) are often used, which determine the mechanical properties by means of a standardized indenter and thus circumvent these problems. Daphalapurkar et al. [26] were one of the first to use nanoindentation measurements directly on closed-cell polymer foams to determine the linear-elastic properties of the foam base material. To reduce the additional compliance due to the porous foam structure, the foam samples were mounted in epoxy resin. Afterwards the specimen surface was polished to create a flat surface for measurement. Chen et al. [11] have also used this method to determine the stiffness of the base material of closed-cell foams made of styrene-acrylonitrile (SAN; foam density ≈ 148 kg/m^3). Marvi-Mashhadi et al. [13] adapted this method for the measurement of low-density closed-cell rigid PUR-foams (foam density ≈ 30 kg/m^3). Due to the low density of the examined PUR foams, embedding the outer pores with resin is not sufficient to fully compensate the influence of the structural compliance. To overcome this limitation, the thickness of the samples was decreased as much as possible (about 1 mm), and the porosity was reduced by means of acryl resin infiltration (Loctite 401) on the open holes on the surface of samples to create more support beneath the corresponding cell triple points (vertices). The specimen surface was polished and indentation was carried out in vertices that appeared on the surface after polishing. The schematic of

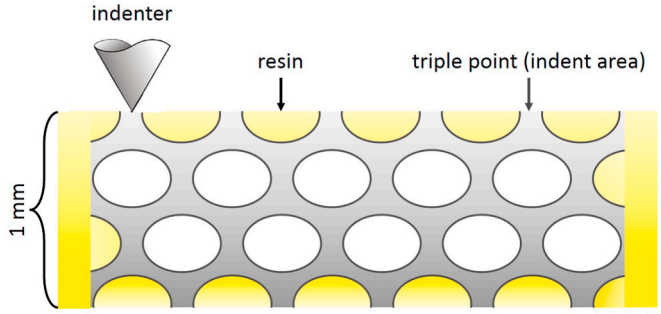

Fig. 4. Schematic of the foam sample for the nanoindentation test according to Ref. [13].

the sample preparation for the instrumented nanoindentation tests is shown in Fig. 4.

Similar tests were carried out on the infiltrated resin within the foam pores, and on the bulk resin specimen. The extra compliance induced by the porosity of the foam was obtained by comparison of the load-penetration curves obtained from the tests on the infiltrated resin in the foam pores, and from the tests on the bulk resin. This extra compliance was subtracted from the load-penetration curves of the PUR foam to correct the influence of the porosity in the foam. The Young's modulus of the PUR foam base material determined by this method is between 2.4 and 2.5 GPa [13,15].

This investigation builds up on the aforementioned measurement methods and the assumption of the varying foam base material in polyisocyanurate-based metal-foam composite elements. For this reason, this study has three main objectives:

1. Analysis of the local chemical composition of PIR foam using ATR-IR spectroscopy with focus on the local PIR content.
2. Evaluation and validation of the different approaches to measuring the mechanical properties of a PIR foam base material by using a compact "foam" sheet (foam system without blowing agent). Atomic force micro-scopy (AFM) and nanoindentation are used as direct measuring methods. To validate these methods, the two direct measuring methods as well as a macroscopic tensile test are performed on the compact sheet. The tensile test serves as reference.
3. Analysis of the local foam properties by a direct measurement method based on the local chemical composition and method evaluation. In parallel, the foam sample preparation used in the state of the art is compared with a new preparation method.

2. Material and experimental techniques

For the investigations, diverse foam samples from three commercially available polyisocyanurate-based metal-foam composite elements of varying thickness (40, 60, and 100 mm) were analyzed in order to consider a possible influence of the panel thickness. All these panels were produced by the same manufacturer and had the same basic formulation (provided by Covestro Deutschland AG in Leverkusen, Germany). It should also be mentioned that the foaming process is carried out exclusively by means of physical blowing agents (*n*-pentane). Nevertheless, unwanted side reactions with water (residual water in polyol or air humidity), which act as chemical blowing agents, cannot be completely excluded.

Measured according to DIN EN ISO 845 10/2009, the foams have an average density of approximately 36-37 kg/m^3 over the entire foam height. In addition, the open cell content of the foams was determined according to DIN EN ISO 4590 and is between 3 and 5%. As a result, 95–97% of the cells are closed.

Table 1
Macroscopic evaluation of the compact "foam" plate.

Method	Machine	Parameters	Results
Uniaxial tensile test (DIN EN ISO 527–1:2012 at 23 °C with speckle pattern and digital image processing)	Zwick HC 10	Young's modulus; Poisson's ratio	E = 3891 ± 55 MPa; ν = 0.38 ± 0.01
Dynamic mechanical analysis (23 °C; 0.1–10 Hz,0.5% strain)	DMA GABO EPLEXOR® Serie Up to ± 500 N	Dissipation factor	tan δ = 0.0299 ± 0.0006

The compact "foam" sheets were produced using the Reaction Injection Molding (RIM) process and a 4 mm thick sheet mold by using the chemical system of the 60 mm thick panel (without blowing agent). It is assumed that the missing physical blowing agent (*n*-pentane) behaves inertly during the foam reaction, and thus comparable reactions occur during the sheet production. Here the maximum mold temperature is approximately 80–90 °C due to the water temperature control and a mold release agent on the plate surface can lead to unwanted reactions, 1 mm was removed from the 4 mm plate on each side after production to avoid any edge effects (see Section 3.1).

The results of the macromechanical evaluation of the compact "foam" sheet, which represent the basis for further investigations, are summarized in Table 1. It can be seen that the examined material is a stiff thermosetting polymer with negligible viscous effects (tan δ ≪ 1). Since the chemical system of the compact sample is comparable to that of the foam, it is assumed that the viscous effects of the foam base material are also negligible.

2.1. Material characterization by means of ATR-IR-Spectroscopy

Infrared (IR) spectra were recorded on a Bruker Vertex 70 mid-infrared spectrometer with a Pike MIRacle ATR unit. A spectral range of 600–4000 cm^{-1} was covered with a resolution of 4 cm^{-1} and 16 scans were averaged per spectrum. A ZnSe ATR crystal was chosen since it allows for low-noise measurements in the relevant spectral window. Before recording the spectra of foams, thin slices of the foam were cut out from the respective positions within the metal panels. Since varying amounts of residual blowing agents can lead to fluctuations in the spectra, the slices were then compressed multiple times to remove the cell gas. Sheets of the compact material were ground to the respective measurement positions, while taking care that the material did not excessively heat up during the process. For both, rigid foam and compact samples, the ATR crystal coverage is not always ideal, leading to varying signal intensities even in repeated measurements on the same sample. Although fluctuating baselines were corrected by subtracting straight lines between selected anchor points (local minima; same points for all spectra), the peak intensities of foams and compact samples can still differ to some extent. For this reason, signal ratios instead of individual signal integrals are relied on when comparing the two sample types (see Section 3.1). This usually allows reliable comparisons as long as the formulation is similar for all samples.

2.2. Nano- and micromechanical characterization of the foam base material

2.2.1. Atomic force microscopy

Atomic Force Microscopy (AFM) offers, in addition to the imaging

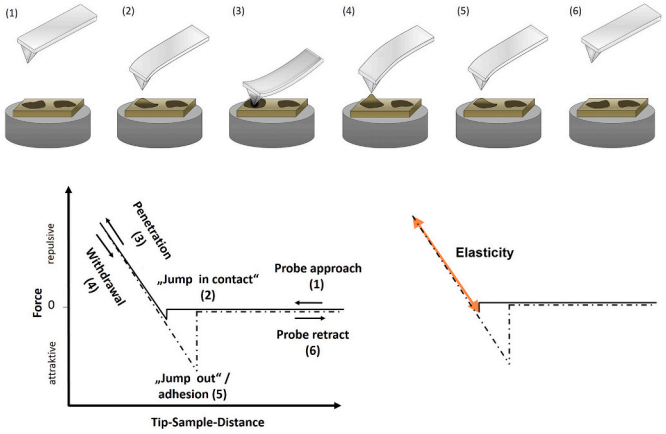

Fig. 5. Curve progression of the force-distance measurement.

measurement technique, the possibility to observe the interactions between the SiO2-AFM tip and the sample as a function of the distance between them using "Fast Force Mapping (FFM)". Fig. 5 shows the curve progression of the force-distance measurement in which the sample and measuring tip first approach vertically, come into contact, and then move away from each other.

To determine the elastic properties, the slope of the load curve (3) is evaluated on the basis of the Hertz model [28], assuming according to Binnig et al. a spherical tip end of the AFM probe [29], which was previously determined using scanning electron microscope images (Fig. 6).

The reduced (or effective) modulus (Er) is obtained as the mechanical parameter. The reduced modulus is a combination of the AFM probe and sample material properties and can be described by the following equation [28,30]:

$$\frac{1}{E_r} = \frac{1-\nu_1^2}{E_1} + \frac{1-\nu_2^2}{E_2} \tag{1}$$

where ν_1 and E_1 are the Poisson's ratio and elastic modulus of the sample, respectively, and ν_2 and E_2 are the Poisson's ratio and elastic modulus of the AFM probe, respectively. However, since the sample is far less stiff than the probe, the elastic modulus of the sample (E_1) can be described as:

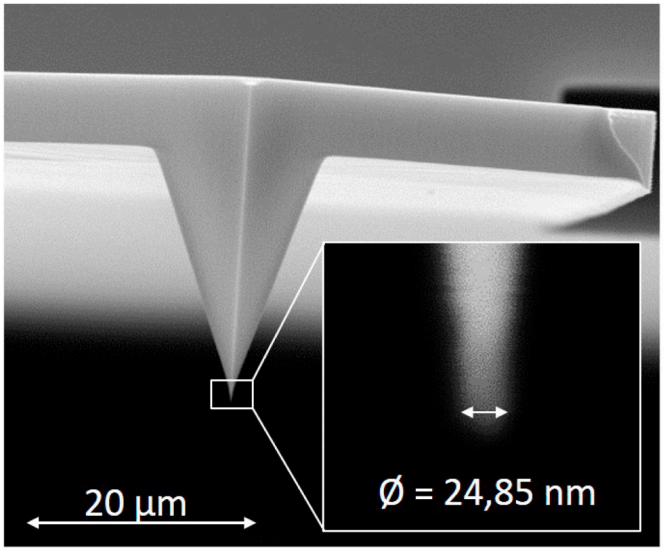

Fig. 6. SEM image of the AFM tip with a radius of 12.4 nm.

$$E_1 = E_r \cdot \left(1-\nu_1^2\right) \tag{2}$$

The foam samples were prepared using a razor blade and fixed on sample carriers. Measurements were carried out on the foam struts. Due to the low forces, it is not necessary to embed the foam. This can be confirmed by the results shown in Section 3.2. The compact sheet was also examined on the cross-section, which was prepared using a microtome and fixed on a sample carrier. For each sample, several measuring points are analyzed. Thereby, the atomic force microscope "Asylum Research Cypher S®" generates 5 µm × 5 µm images with a lateral resolution of 19.5 nm. The 256 force-distance curves per row and column are recorded with a scanning speed of 0.8 Hz (quasi-static) and a maximum specified force of 600 nN.

2.2.2. Nanoindentation

In nanoindentation, a probe is brought into contact with a surface, pushed into the material, and retracted, while the load (P), displacement (h), and time (t) are recorded. Based on the selected probe and P–h–t curves, multiple models exist to extract mechanical properties depending on the deformation modes of the indented material. These diverse analysis models, in combination with the selected measurement parameters, can lead to significantly different results [31]. For this reason, suitable settings must first be found which provide comparable results to the macroscopic tensile tests.

Due to their distinct viscoelasticity, polymers are often evaluated using visco-elastic (VE) or visco-elastic-plastic (VEP) methods. However, since the viscous effects of the compact sample (or foam base material) are negligible (see Table 1), the most widely used elastic-plastic model based on the Oliver-Pharr (OP) method [32,33] is chosen for this investigation. This method is much less complex and error-prone than the viscous models [31]. In the OP method, the reduced modulus is calculated from the unloading curve of the P-h-plot (Fig. 7a) based on the assumption that the unloading response is purely elastic. The reduced modulus can be described as:

$$E_r = \frac{S\sqrt{\pi}}{2\beta\sqrt{A_c}} \tag{3}$$

where the stiffness at peak load (S) is calculated as the slope of the unloading curve, the contact area (Ac) is the projected area obtained via a calibration function and β is a dimensionless parameter that depends on the indenter geometry.

Like the AFM measuring method, the reduced modulus is described by the mechanical properties of the sample and the indenter. Consequently, Eq. (2) from Section 3.2 can also be used here to determine the Young's modulus of the material [34].

Especially with stiff materials, very good agreement to macroscopic values can be observed by using the OP approach [35–37], while modulus values for polymeric materials that have distinct viscoelasticity are often overestimated [38,39]. Nevertheless, also polymers with low viscoelasticity can be evaluated by this method. The influence of the viscous error can be partly compensated by using a three-stage (trapezoidal) loading protocol. The (dwell) period used is common practice to ensure that the relief reaction is purely elastic [40,41]. Therefore all subsequent indentation experiments were performed on a Bruker Hysitron TI Premier® nanoindenter using the mentioned three-stage load--controlled protocol, which is shown in Fig. 7b. Furthermore, quasi-static measurements at ambient temperature (296 K ± 2 K) are performed based on the latest literature [13], which deals with the direct determination of the properties of the foam base material.

For the first validation tests on the compact samples, which were prepared using a microtome and fixed on sample carriers, the influence of the selected indenter was examined. For this purpose, a spherical diamond indenter (1 µm diameter; often used for soft polymers) and a diamond pyramidal Berkovich indenter (most widely used indenter) were used. The calibration of the indenters was performed on fused

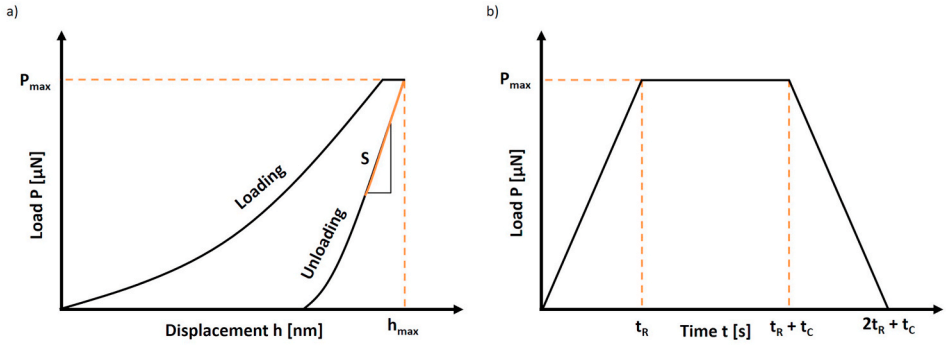

Fig. 7. (a) Load-displacement curve and (b) Trapezoidal load function. Loading to peak load (P_{max} = 800 µN) during rise time (t_R = 15 s) with a creep hold (t_C = 60 s) before unloading. Same loading and unloading rate ($k = P_{max}/t_R$).

silica and polycarbonate. In order to investigate the dependence of the determined modules on the maximal peak load (or penetration depth), measurements in 100 µN steps from 200 to 1000 µN were carried out in preliminary tests on the compact samples and later on the prepared foam samples. For each measuring force setting 6 repetitions were carried out. It was observed that stable values could be achieved in the peak load range from 600 to 1000 µN for all test setups. For this reason, a maximum peak load of 800 µN was chosen for all further investigations.

For the analysis of the local mechanical foam properties, the indenter with the smallest deviation of the Young's modulus compared to the macroscopic tensile test was selected. Additionally, two different foam sample preparations were compared. One of these preparation methods is based on the methodology by Marvi-Mashhadi et al. (Fig. 4). The only two differences to the method described above are that the foam samples are embedded into thermo-set epoxy resin of high stiffness to reduce compliance and are cut using a microtome after curing and not polished. In the following course of this work, this preparation method is referred to as "Literature preparation method (LPM)".

In contrast to the LPM, in which an intact, thin foam strip is embedded, the new method involves embedding tiny foam fragments (same embedding agent as LPM). Hereby possible errors (statistical spread and compliance) due to incompletely embedded foam cells should be avoided (Fig. 8). After curing the foam samples are also cut using a microtome and fixed on sample carriers. The indentation was carried out on the foam fragments that appear on the surface after cutting. In the following course of this work, this preparation method is referred to as "New preparation method (NPM)".

In addition to measurements on the foam base material (vertices or fragments), similar tests were carried out on the infiltrated resin within the foam pores, and on the bulk resin specimen to evaluate and, if necessary, correct the influence of porosity or embedding. For the measurements on the base material and embedding agent, at least 10 repetitions per test point were performed.

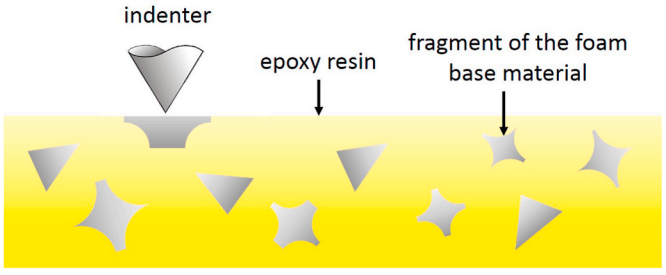

Fig. 8. Schematic of the "New preparation method (NPM)".

3. Experimental results and discussion

3.1. ATR-IR-spectroscopy

The IR spectra were used to analyze the distribution of isocyanurates and other reaction products throughout the parts. As outlined above, the reaction temperatures differ within metal panels during production. While the core region of the foams reaches up to ca. 150 °C due to the exothermic reactions, the peak temperatures are much lower close to the metal sheets. As mentioned above, the latter are usually pre-heated to ca. 60 °C so that they effectively cool the material while the reactions proceed. Since the activation barrier for forming isocyanurates is much higher than for e.g. urethane groups, a higher concentration of the former builds up in the core region.

Several signals in the IR spectra reflect this gradient in reaction temperature during processing (Fig. 9). As expected, the most pronounced intensity variations are observed in the isocyanurate signals at ca. 1410 cm^{-1} and 1705 cm^{-1} (ring vibration and carbonyl stretch vibration, respectively). Both signals overlap with other bands in the spectrum, which makes a quantitative analysis of the isocyanurate content challenging. However, this content can be compared in a relative fashion within a part and among diverse samples with the same formulation. As indicated in Section 2.1, the ratio of two product signals is used here as an indicator for the local PIR content. This way, the shape of the distribution in Fig. 10 remains virtually identical to the one of the pure PIR signal intensities. However, the ratio allows for a direct comparison between foam and compact sample spectra even if the coverage of the ATR-IR crystal differs. The ratio of the strong PIR signal at 1405 cm^{-1} to an Amide III type signal around 1220 cm^{-1} was chosen here. The latter is an indicator for the local urethane and/or allophanate

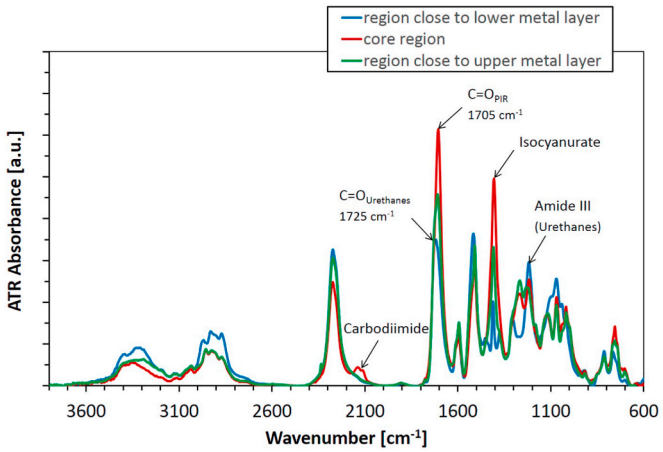

Fig. 9. Exemplary set of IR spectra for the 60 mm thickness metal panel foam.

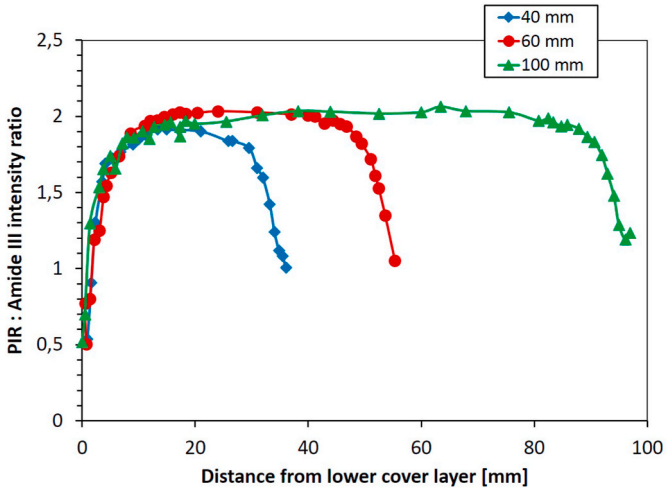

Fig. 10. Height-resolved PIR: Amide III intensity ratio of the different foam samples as a measure of the local PIR content. To calculate the ratio, the signals were integrated between 1350 and 1470 cm^{-1} and 1190–1245 cm^{-1}, respectively. The baselines for integration were drawn between these points.

concentrations.

Analyzing the spectra of the metal panels with 40, 60, and 100 mm thickness along their height, it becomes obvious that only the first 10–15 mm from each metal sheet are affected by external cooling effects (Fig. 10). In this range, the PIR signal intensity increases drastically with increasing distance to the metal sheets. A comparison of the boundary values shows that the intensity of the PIR signal is lower at the lower cover layer for each metal sheet than at the upper one. The reason for this could be the polyurethane-based adhesion promoter, which is applied to the lower cover sheet (Fig. 2). More likely, the foam at the upper cover layer will reach a higher temperature during the process. This can be justified by the different heat exchange. While the lower foam is in direct contact with the metal cover layer and thus the exothermic heat is transferred to the metal cover layer by heat conduction, the foam at the upper cover layer first loses its heat more slowly by convection during foaming.

At distances greater than ca. 15 mm from each sheet, the PIR signal and the spectra in general exhibit a constant shape. It can be deduced that the temperature evolution during production is similar for any position within this core region of the foam, i.e., the reactions occur under quasi-adiabatic conditions. This observation is confirmed by the identical slopes of the signal intensities within the first 15 mm of each panel and by the virtually identical signal intensities within the three plateau regions. It also means that the chemical composition of the foams is virtually identical for both, the first 15 mm from the sheets and the plateau regions of all three panels. Thus, it can be expected that the mechanical properties of the respective foam base materials are close to identical as well. It is therefore sufficient to study only one of the three panels in more detail. The 60 mm thickness panel was selected for this purpose. To derive a possible correlation between the PIR content and the mechanical properties of the foam base material in the further course

Table 2
PIR: Amide III intensity ratio of 60 mm thickness metal panel foam at defined positions.

Distance lower cover layer [mm]	PIR: Amide III intensity ratio
0	0.52
5	1.62
10	1.92
20	2.02
30	2.03
60	1.10

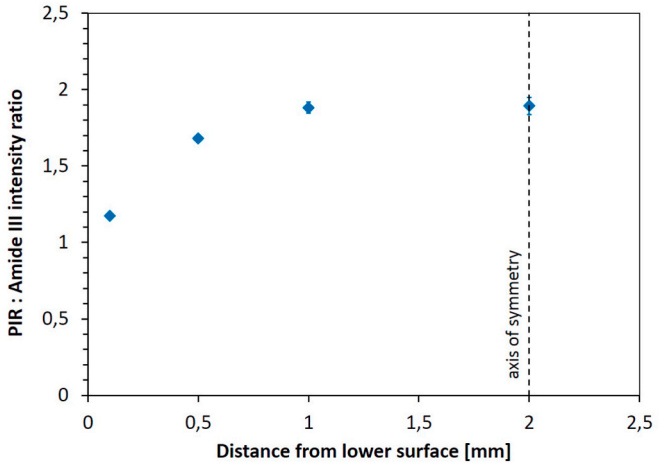

Fig. 11. Height-resolved PIR: Amide III intensity ratio of the 4 mm thick compact sample.

of this work, Table 2 shows the PIR: Amide III ratios of selected positions. At these positions the following measurements of the Young's modulus are also performed.

As detailed above, 4 mm thick compact samples of the PIR material were produced by removing all blowing agents from the formulation and curing in a pre-heated steel mold at 80 °C. IR spectroscopy was used to check whether the chemical composition and in particular the PIR content was similar to the metal panel foams. As expected, the walls of the mold appear to have a similar cooling effect on the reactive material as the metal sheets have on the foaming material. However, the affected region is much smaller, i.e. only material within less than ca. 1 mm from the walls seems to be affected (Fig. 11). Judged by the spectra, the inner 2 mm of the compact samples have a constant chemical composition. Also, with the production procedure followed here, the PIR content in this region is similar to the one in the metal panels plateau regions. So, the mechanical properties of the two polymer materials should be comparable. For further analysis of the compact samples and direct comparison to the metal panel foam cores, only the inner 2 mm of the material were used. For this purpose, 1 mm was ground off from each side of the compact sheets.

3.2. *Atomic force microscopy*

The results of the height-resolved AFM measurements on the 60 mm foam sample and the compact plate are shown in Fig. 12. The Young's

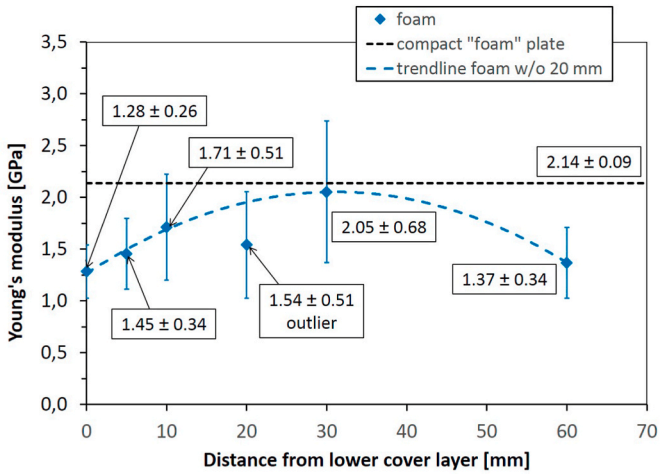

Fig. 12. AFM Young's modulus.

moduli used were converted from the reduced moduli using the Poisson's ratio of the compact plate (see Table 1 and Eq. (2)).

It can be seen that the Young's modulus increases from the outer cover layers towards the center of the panel. Only the value at 20 mm deviates from the rising trend and is therefore regarded as an outlier and not further considered. In the vicinity of the metal sheets only values of approx. 1.3–1.4 GPa were measured, whereas the value at the upper cover layer has a slightly higher value. This can be explained by the different PIR content (see Section 3.1). In the center of the panel the modulus is at the level of the compact PUR/PIR material (≈ 2.1 GPa). This confirms the assumption from the IR evaluation that the material in the foam center and the compact sample are chemically and mechanically comparable, and no embedding of the foam is necessary due to the very small loads.

Furthermore, high scattering of the values can be observed, which increase from the cover layers to the center of the foam with increasing Young's modulus. The high scattering can be explained by the high resolution of the AFM method, which is able to detect the individual components on a scale of a few nanometers. A possible reason for the increase in scattering towards the foam center could be a changed PUR/

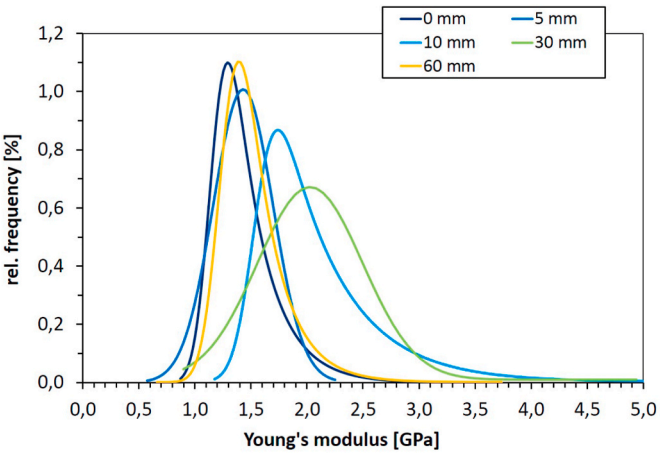

Fig. 14. Young's modulus distribution of foam struts at different height.

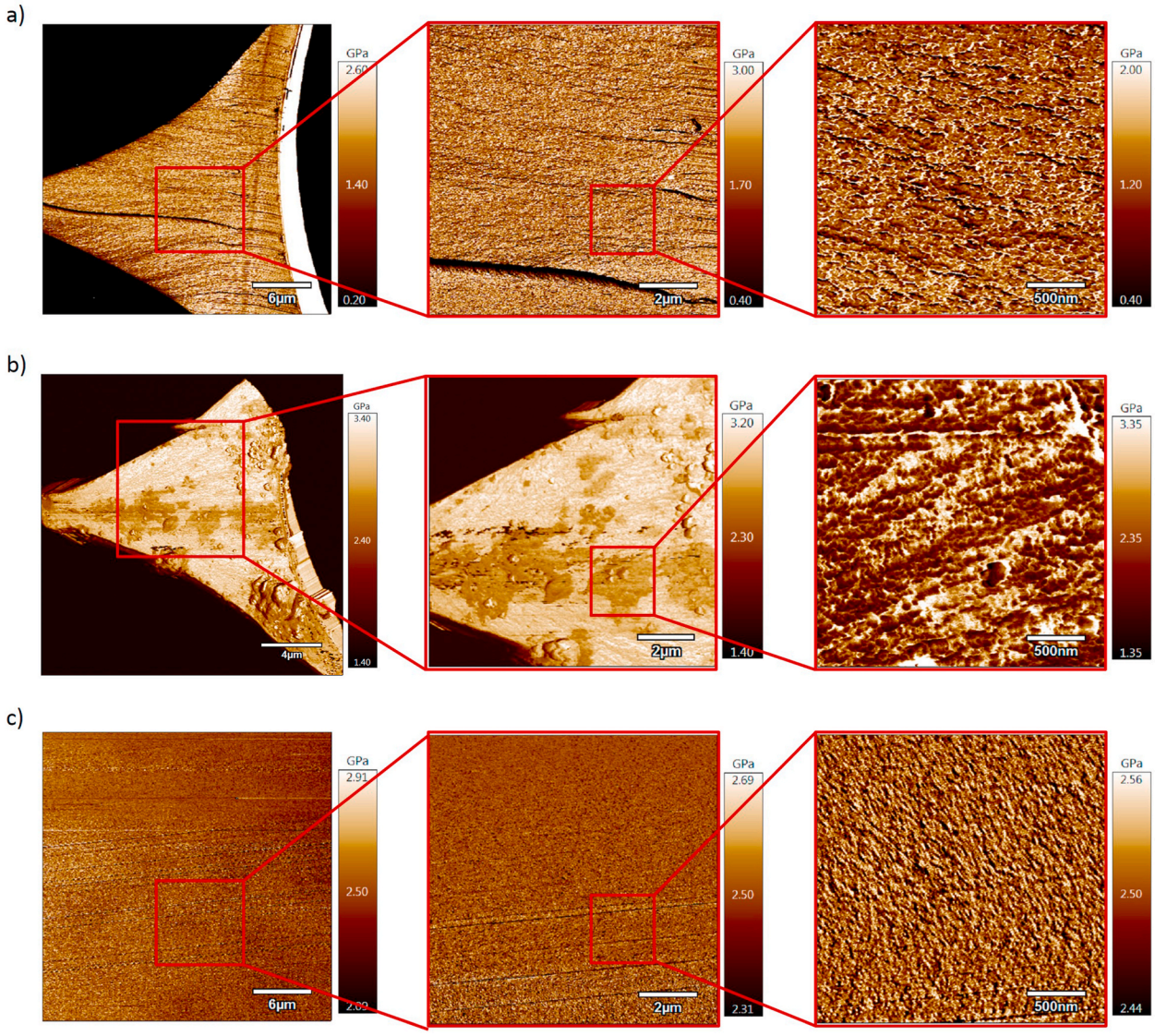

Fig. 13. AFM images of the morphological arrangement of the hard-/soft segments in different foam strut cross-sections and compact sample by showing the distribution of the reduced module. (a) Foam strut at a distance of 0 mm from the lower cover layer, (b) Foam strut at a distance of 30 mm from the lower cover layer, and (c) Compact sample.

PIR ratio. This hypothesis is supported by the morphological arrangement of the harder and softer segments in the foam strut cross-section, which are represented by distribution of the reduced module by means of AFM images. While in the images of the foam struts near the cover layers a more uniform structure is visible (Fig. 13a), coarser segregations (probably accumulations of the individual PUR/PIR components) can be seen especially in the foam struts at a distance of 30 mm from the lower cover plate (Fig. 13b). Compressions and cracks within the foam struts are caused by the preparation.

An additional indication of the above-mentioned hypothesis can be deducted by observing the respective Young's modulus distribution of the foam struts at different heights (Fig. 14). While the Young's moduli of the struts are normally distributed near the cover layers (0, 5, and 60 mm), as PUR is primarily formed there (see Section 3.1), a log-normal distribution can be observed at a distance of 10 mm. This suggests that larger quantities of PIR are formed and thus the distribution is shifted to higher values on one side. In the center of the foam sample (30 mm), where the PIR content has further increased, a distinct PUR/PIR mixing phase has formed, so that the values are normally distributed again.

Interestingly, a comparatively small scattering of the values is observed in the compact sample, although the PIR content is similar to that in the foam center. Besides, a very homogeneous distribution of hard/soft segments and PUR/PIR components can be observed (Fig. 13c). This could be explained by the manufacturing process, in which the more homogeneous temperature ($\hat{=}$ more uniform reaction), the increased pressure in the mold and the absence of a foaming process prevents accumulations of the individual PUR/PIR components.

If the value of the compact plate from the AFM measurement is compared with those from the macroscopic tensile test, it is noticeable that the AFM value provide a significantly lower value. This deviation can be explained by the three following reasons:

1. Distinct size effect between the measurement methods
2. Assuming a perfectly round AFM tip is not correct
3. Selected evaluation model may not be suitable

As a result, these values from the AFM method cannot be directly transferred to macroscopic measurement values. Nevertheless, a qualitative evaluation of the local properties can be made using these AFM values (stiffness increases with increasing PIR content). Furthermore, it can be tried to correct the deviation by introducing a correction factor. In this case, a constant factor between the AFM module and the tensile module is determined on the basis of the compact plate. In our case, this factor is 1.82 ($E_{AFM}/E_{Tensile}$). Subsequently, this factor is applied to the foam values. The results are shown in Table 3.

It should be mentioned that a material-independent factor is assumed, which can only serve as a first approximation for this case.

3.3. Nanoindentation

The results on the influence of the indenter on the reduced modulus (Er) of the compact plate are shown in Table 4. Like the AFM evaluation, the reduced moduli were converted to Young's moduli (E) using the measured Poisson's ratio and Eq. (2). For comparison, Young's modulus of the macroscopic tensile test is also shown in the Table.

Table 3
Macroscopic evaluation of the compact "foam" plate.

Distance lower cover layer [mm]	Corrected AFM Young's modulus [GPa]
0	2.33
5	2.64
10	3.11
30	3.73
60	2.49

Table 4
Results nanoindentation and tensile test on compact sample.

Method	Reduced modulus [GPa]	Young's modulus [GPa]
Nanoindentation (Berkovich)	4.58 ± 0.10	3.92 ± 0.09
Nanoindentation (Spherical)	3.10 ± 0.09	2.65 ± 0.08
Macroscopic tensile test	–	3.89 ± 0.06

If Young's moduli of the compact plate from the nanoindentation measurement are compared with those from the macroscopic tensile tests, it becomes clear that the nanoindentation using the Berkovich indenter provides very similar values to those of the tensile test (3.89 GPa; deviation $\leq$ 1%). The Young's modulus of the spherical indenter is significantly lower than the value obtained in the tensile test. Based on these results, the Berkovich indenter will be used for further investigations.

In the following, the two embedding methods LPM and NPM (see Section 2.2.2) are evaluated and compared at the foam center (30 mm). Since the material in the foam center is similar to the compact sample (see results of ATR-IR and AFM), the nanoindentation value (Berkovich) of the compact sample was used as an evaluation criterion for the embedding.

The results of both embedding methods are shown in Table 5 and Fig. 15. Table 5 lists the resulting mean values including standard deviation from the foam sample and the compact sample. Fig. 15 represents the individual measurements on the foam struts, the embedding next to the foam struts, and the reference (bulk) embedding (slight fluctuations in the reference embedding values are due to the manual production method). If the mean values of the embedding next to the foam struts and the reference embedding from the LPM embedding from Table 5 are considered first, no correction of the structural compliance seems to be necessary, since both values are very similar.

However, by looking at the individual measurements in Fig. 15a it becomes clear that an exact correction is not possible at all. This can be justified by the fact that in some cases the values of the embedding next to the foam struts clearly exceed the values of the reference medium (see indents 2 and 4). The stiff foam material may cause the measurements on the less stiff embedding medium to be influenced and therefore a higher value is measured. This effect cannot be excluded even with the less distinct or non-visible measuring points. This influence and the resulting impossibility of compliance correction can also explain why the values from the foam are significantly below the value of the compact plate and have a similar mean value to the embedding next to the foam struts.

Furthermore, it has been shown that the measurements of the LPM embedding are subject to strong fluctuations. The reason for this is, on the one hand, the non-uniform or partially incomplete embedding of the cell struts due to the closed-cell structure (Fig. 16a) and, on the other hand, the non-embedded, variable foam structure beneath the foam struts (Fig. 4). In comparison, the scattering of the foam strut values is significantly lower with the NPM embedding. Fig. 16b shows that most of the foam struts are completely embedded and only a few small defects

Table 5
Results of the different embedding methods (LPM and NPM) at the foam center (30 mm).

Method	Young's modulus [GPa]		
	Foam bulk material	Embedding next to foam struts	Reference embedding
Nanoindentation foam 30 mm LPM	3.42 ± 0.41	3.32 ± 0.28	3.35 ± 0.05
Nanoindentation foam 30 mm NPM	3.93 ± 0.09	3.34 ± 0.11	3.16 ± 0.10
Nanoindentation compact sample	3.92 ± 0.09	–	–

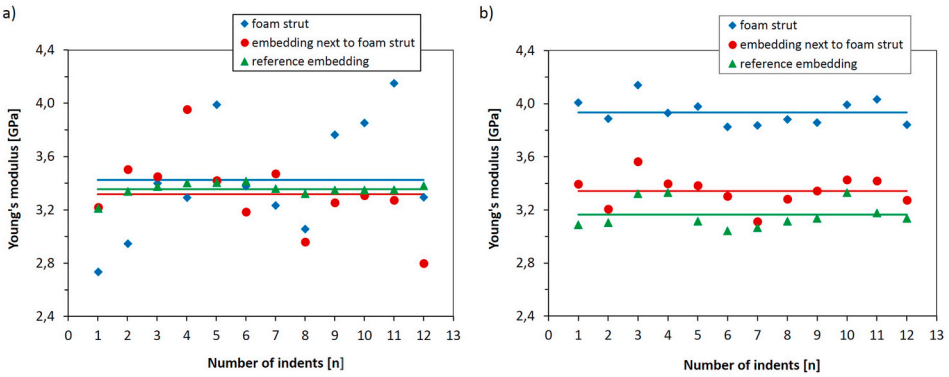

Fig. 15. Young's moduli of foam struts, embedding next to foam struts and reference embedding of the foam sample at 30 mm using (a) LPM and (b) NPM.

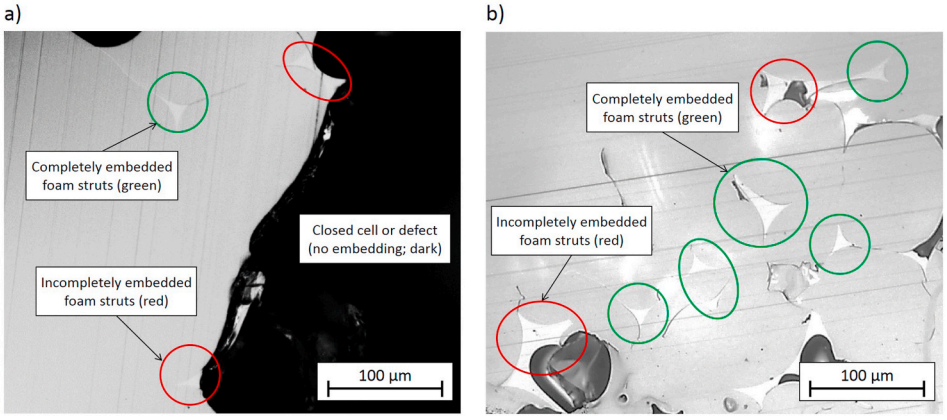

Fig. 16. SEM images of the different embedding methods (a) LPM and (b) NPM. LPM embedding has significantly more incompletely embedded foam struts than completely embedded foam struts. With the new embedding method (NPM), the ratio is reversed and the spatial concentration is significantly higher.

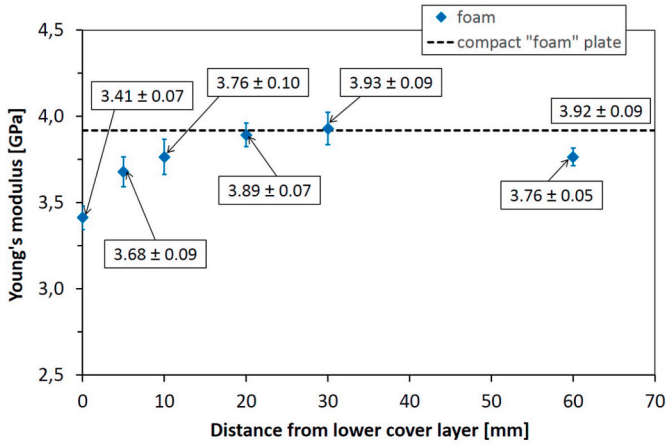

Fig. 17. Nanoindentation Young's modulus.

occur. Besides, it can be assumed that the structure beneath the struts is also embedded and is therefore much more stable and uniform. Correspondingly, no correction of the compliance has to be carried out. This is also shown by the mean value of the measured foam strut Young's modulus (3.93 ± 0.09 GPa), which is very close to that of the compact plate. Consequently, the new embedding method (NPM) represents a significant improvement over the embedding method from the literature (LPM).

Based on these results, the remaining height-resolved measurements on the foam sample are performed with the NPM embedding. The results are shown in Fig. 17. As with the AFM method values, the Young's modulus increases from the outer cover layers to the center of the panel, but the differences are not as distinctive (maximum difference between 0 mm and 30 mm is ≈ 15 %.). Of particular interest is the significant difference between the boundary values. A Young's modulus of 3.41 GPa is measured at the lower cover layer (0 mm). At the upper cover layer (60 mm), a Young's modulus of 3.76 GPa is measured, which corresponds to the value at 10 mm. As mentioned earlier, these differences can be explained by the adhesion promoter on the one hand and by the different temperatures on the other hand.

In contrast to the AFM method, the nanoindentation is not able to

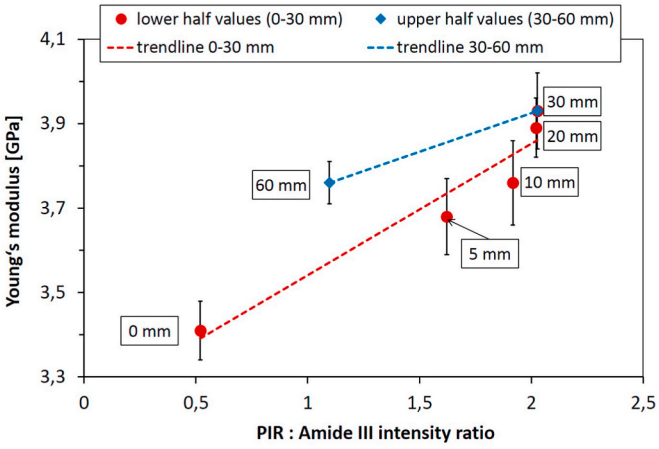

Fig. 18. Correlation PIR: Amide III intensity ratio and Young's modulus.

resolve the individual harder and softer segments due to the larger tip dimension. Therefore, no change of the standard deviations due to varying PUR/PIR ratios at different positions can be detected.

3.4. Correlation PIR content and Young's modulus

In this section, the correlation between the local PIR content (estimated by the PIR: Amide III intensity ratio; Section 3.1) and the corresponding Young's modulus is investigated. Since it can be assumed that the values of the nanoindentation provide more realistic results, the Young's moduli from Section 3.3 are used for this investigation. Fig. 18 shows the results of the correlation.

From the comparison of the values to be correlated, it is noticeable that no uniform correlation can be recognized for the total foam height (0 mm–60 mm). The reason for this are the values at the position 60 mm. There the Young's modulus is at the same level as at the position 10 mm, but the value of the PIR content is significantly lower. Consequently, it appears that in addition to the local PIR content, there are other, currently unknown characteristic values that significantly influence the mechanical properties of the foam base material, which may be influenced by the process (e.g. application of adhesion promoter on the lower cover layer). Nevertheless, it can be shown that a higher PIR content tends to lead to an increase in the Young's modulus. This effect becomes even more apparent if the values of the foam are considered separately for the upper and lower foam half. First, the values of the lower foam half are evaluated (0 mm–30 mm). Here a linear relationship can be seen as a first approximation. For the upper foam half only the values at the position 60 mm are known besides the values in the foam center (30 mm). However, if it is assumed that the intermediate positions, similar to the lower half, decrease approximately linearly from the foam center to the upper end, a first linear approximation can be performed here as well. It should be mentioned again that the correlations shown, especially for the upper half of the foam, can only give a first tendency so far and further investigations are recommended.

4. Conclusion

It is shown that the chemical composition of PIR foams changes significantly depending on the height. As a special parameter the PIR: Amide III intensity ratio is to be mentioned, which was determined using ATR-IR spectroscopy and represents the quantity of the formed PIR groups. Due to chemical and process-related effects, the proportion of PIR groups increases steadily from the outter cover layers to the foam center. Interestingly, the PIR content is higher at the upper cover sheet than at the lower one. This can be explained by the application of the adhesion promoter and the different heat flow. Based on the local chemical composition, defined positions on the foam were investigated using the AFM and nanoindentation method to determine the mechanical properties (Young's modulus) of the foam base material. With both measuring methods, an increase of the Young's modulus towards the foam center is detected. However, it has been shown that the results of the AFM method deviate significantly from the macroscopic values and are also subject to large scattering. Therefore this method is only suitable for qualitative evaluation. Interestingly, previously unknown local segregations in the cell struts could be observed by means of the AFM imaging measurement technique. A better understanding of the formation of these segregations could be used to adjust the metal panel recipes in order to consciously create or prevent segregations and thus control the overall properties.

For the measurements using nanoindentation, a new embedding method was developed, which achieves significantly more realistic and reproducible results compared to the embedding used in the literature and shows a very good agreement with the macroscopic values. Based on these values, an attempt was made to find a correlation between the local PIR: Amid III intensity ratio and the corresponding Young's modulus. A correlation for the total foam height could not be found. Therefore it seems that there are other, currently unknown, characteristic values besides the PIR: Amide III intensity ratio, which influence the mechanical properties. A possible reason for these differences could be the application of the adhesion promoter on the lower cover layer. This could also explain why as a first approximation a separate linear correlation can be formed for the upper and lower foam half. These approximations make it clear that a higher PIR: Amid III intensity ratio leads to an increase in the Young's modulus. However, it must be mentioned that these correlations can only serve as a first tendency and further investigations are recommended.

Declaration of competing interest

The authors declare the following financial interests/personal relationships which may be considered as potential competing interests: This investigation was financially supported by the Covestro Deutschland AG which is gratefully acknowledged.

Acknowledgement

This investigation was financially supported by the Covestro Deutschland AG which is gratefully acknowledged.

References

[1] H. Keller, Strukturbildung in Polyurethandispersionen und -filmen, PhD thesis, Johannes Gutenberg-Universität Mainz, 2014.
[2] U.E. Stempel, Dämmen und Sanieren in Alt- und Neubauten, Franzis Verlag GmbH, 2011.
[3] J. Anderson, U. Cabulis, L. Stiebra, M. Kirpluks, E. Sparnins, Modeling the mode i fracture toughness of anisotropic low-density rigid pur and pir foams, Int. J. Fract. 205 (2017) 111–118.
[4] R. Schlimper, Verformungs- und Versagensverhalten geschlossenzelliger Polymerhartschäume, PhD thesis, Martin Luther-Universität Halle-Wittenberg, 2014.
[5] D. Zenkert, The Handbook of Sandwich Construction, Engineering Materials Advisory Services Limited, 1997.
[6] A. Al Nabulsi, D. Cozzula, T. Hagen, W. Leitner, T.E. Müller, Isocyanurate formation during rigid polyurethane foam assembly: a mechanistic study based on in situ ir and nmr spectroscopy, Polym. Chem. 9 (2018) 4891–4899.
[7] N. Adam, G. Avar, H. Blankenheim, W. Friedrichs, M. Giersig, F. Weigand, M. Halfmann, F.W. Wittbecker, D.R. Larimer, U. Maier, S. Meyer-Ahrens, K. L. Noble, H.G. Wussow, Ullmann's Encyclopedia of Industrial Chemistry - Polyurethanes, Wiley-VCG Verlag GmbH & Co. KGaA, 2012.
[8] E. Calgua, Verbundelement, enthaltend einen polyurethanhaftvermittler, 2005, p. 5. https://worldwide.espacenet.com/DE10343902A1. Patent number: DE10343902A1.
[9] J. van de Braak, T. Rüb, Vorrichtung und verfahren zur herstellung von sandwichverbundelementen, 2005, p. 11. https://worldwide.espacenet.com/DE102004022677A1. Patent number: DE102004022677A1.
[10] H. Ehbing, I. Kellerhof, C. Möhlenkamp, R. Rauhaus, Method and Apparatus for the Continuous Manufacturing of Foam Boards, 2006, p. 9. https://worldwide.espacenet.com/EP1700682A2. Patent number: EP1700682A2.
[11] Y. Chen, R. Das, M. Battley, Effects of cell size and cell wall thickness variations on the stiffness of closed-cell foams, Int. J. Solid Struct. 52 (2015) 150–164.
[12] C. Lautensack, Fitting three-dimensional laguerre tessellations to foam structures, J. Appl. Stat. 35 (9) (2008) 985–995.
[13] M. Marvi-Mashhadi, C.S. Lopes, J. LLorca, Modelling of the mechanical behavior of polyurethane foams by means of micromechanical characterization and computational homogenization, Int. J. Solid Struct. 146 (2018) 154–166.
[14] M. Marvi-Mashhadi, C.S. Lopes, J. LLorca, Effect of anisotropy on the mechanical properties of polyurethane foams: an experimental and numerical study, Mech. Mater. 124 (2018) 143–154.
[15] M. Marvi-Mashhadi, C.S. Lopes, J. LLorca, Surrogate models of the influence of the microstructure on the mechanical properties of closed- and open-cell foams, J. Mater. Sci. 53 (2018) 12937–12948.
[16] M. Ridha, Mechanical and Failure Properties of Rigid Polyurethane Foam under Tension, PhD thesis, National University of Singapore, 2007.
[17] Y. Chen, R. Das, M. Battley, An approach for characterising cellular polymeric foam structures using computed tomography, in: AIP Conference Proceedings, 2018.
[18] R. Landers, J. Venzmer, T. Boinowitz, Methods for cell structure analysis of polyurethane foams, in: Proceedings of the Polyurethane Conference(API), 2007.
[19] J. Andersons, M. Kirpluks, L. Stiebra, U. Cabulis, Anisotropy of the stiffness and strength of rigid low-density closed-cell polyisocyanurate foams, Mater. Des. 92 (2016) 836–845.
[20] C. P Chen, W.B. Anderson, R. Lakes, Relating the properties of foam to the properties of the solid from which it is made, Cell. Polym. 13 (16–32) (1994), 01.

[21] U. Cabulis, I. Sevastyanova, J. Anderson, I. Beverte, Rapeseed oil-based rigid polyisocyanurate foams modified with nanoparticles of various type, Polimery 59 (2014) 207–212.
[22] A. Kraatz, Anwendung der Invariantentheorie zur Berechnung des dreidimensionalen Versagens- und Kriechverhaltens von geschlossenzelligen Schaumstoffen unter Einbeziehung der Mikrostruktur, PhD thesis, Martin-Luther-Universität Halle-Wittenberg, 2007.
[23] L. Gong, S. Kyriakides, W.Y. Jang, Compressive response of open-cell foams. part i: morphology and elastic properties, Int. J. Solid Struct. 42 (5) (2005) 1355–1379.
[24] D. Tranchida, S. Piccarolo, M. Soliman, Nanoscale mechanical characterization of polymers by afm nanoindentations: critical approach to the elastic characterization, Macromolecules 39 (13) (2006) 4547–4556.
[25] J. Zhou, S. Allameh, W.O. Soboyejo, Microscale testing of the strut in open cell aluminum foams, J. Mater. Sci. 40 (2005) 429–439.
[26] N.P. Daphalapurkar, J.C. Hanan, N.B. Phelps, H. Bale, H. Lu, Tomography and simulation of microstructure evolution of a closed-cell polymer foam in compression, Mech. Adv. Mater. Struct. 15 (8) (2008) 594–611.
[27] L.J. Gibson, M.F. Ashby, Cellular Solids - Structure and Properties, Cambridge University Press, 2001.
[28] H. Hertz, Über die Berührung fester elastischer Körper, J. für die Reine Angewandte Math. (Crelle's J.) 92 (1882) 156–171.
[29] G. Binnig, C.F. Quate, C. Gerber, Atomic force microscope, Phys. Rev. Lett. 56 (1986) 930–933.
[30] E. Broitman, Indentation hardness measurements at macro-, micro-, and nanoscale: a critical overview, Tribol. Lett. 65 (2016) 23–40.
[31] N. Rodriguez-Florez, M. L Oyen, S. J Shefelbine, Insight into differences in nanoindentation properties of bone, Journal of the Mechanical Behavior of Biomedical Materials 18 (2013) 90–99.
[32] W.C. Oliver, G.M. Pharr, Measurement of hardness and elastic modulus by instrumented indentation: advances in understanding and refinements to methodology, J. Mater. Res. 19 (1) (2004) 3–20.
[33] W.C. Oliver, G.M. Pharr, An improved technique for determining hardness and elastic modulus using load and displacement sensing indentation experiments, J. Mater. Res. 7 (6) (1992) 1564–1583.
[34] M.R. VanLandingham, J.S. Villarrubia, W.F. Guthrie, G.F. Meyers, Nanoindentation of polymers: an overview, Macromol. Symp. 167 (1) (2001) 15–44.
[35] E.G. Herbert, W.C. Oliver, G.M. Pharr, Nanoindentation and the dynamic characterization of viscoelastic solids, J. Phys. Appl. Phys. 41 (7) (2008).
[36] E.G. Herbert, W.C. Oliver, A. Lumsdaine, G.M. Pharr, Measuring the constitutive behavior of viscoelastic solids in the time and frequency domain using flat punch nanoindentation, J. Mater. Res. 24 (3) (2009) 626–637.
[37] G. M Odegard, T.S. Gates, H.M. Herring, Characterization of viscoelastic properties of polymeric materials through nanoindentation, Exp. Mech. 45 (2005) 130–136.
[38] A.H.W. Ngan, H.T. Wang, B. Tang, K.Y. Sze, Correcting power-law viscoelastic effects in elastic modulus measurement using depth-sensing indentation, Int. J. Solid Struct. 42 (5) (2005) 1831–1846.
[39] D. Tranchida, S. Piccarolo, J. Loos, A. Alexeev, Mechanical characterization of polymers on a nanometer scale through nanoindentation. a study on pile-up and viscoelasticity, Macromolecules 40 (4) (2007) 1259–1267.
[40] J. Dean, J.M. Wheeler, T.W. Clyne, Use of quasi-static nanoindentation data to obtain stress-strain characteristics for metallic materials, Acta Mater. 58 (10) (2010) 3613–3623.
[41] M.L. Oyen, R.F. Cook, Load-displacement behavior during sharp indentation of viscous-elastic-plastic materials, J. Mater. Res. 18 (1) (2003) 139–150.

Update

Polymer Testing

Volume 100, Issue , August 2021, Page

DOI: https://doi.org/10.1016/j.polymertesting.2021.107234

Polymer Testing 100 (2021) 107234

Contents lists available at ScienceDirect

Polymer Testing

journal homepage: www.elsevier.com/locate/polytest

Corrigendum to' Experimental multi-scale approach to determine the local mechanical properties of foam base material in polyisocyanurate metal panels' [Polym. Test. 93 (2021) 106965]

P. Gahlen [a,*], S. Fröbel [a], A. Karbach [b], D. Gabriel [b], M. Stommel [c]

[a] Covestro Deutschland AG, Kaiser-Wilhelm-Allee 60, 51373, Leverkusen, Germany
[b] Currenta GmbH & Co. OHG, Kaiser-Wilhelm-Allee 50, 51373, Leverkusen, Germany
[c] Leibniz-Institut für Polymerforschung Dresden e.V. (IPF), Hohe Straße 6, 01069, Dresden, Germany

The authors regret that in some figures (Fig. 6, 10, 11, 12, 14, 15, 17 & 18) formatting errors occurred due to the automatically selected language package in Office. The decimal point in the axis labels of the diagrams were accidentally separated with a comma instead of a point. However, since in most cases the values are also displayed explicitly in a table or the diagram, this should not have any effect on the results. The corrected figures are provided below.

The authors would like to apologise for any inconvenience caused.

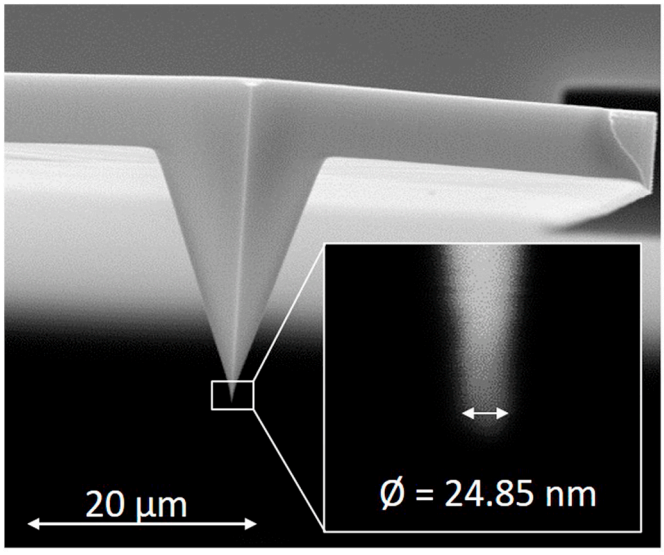

DOI of original article: https://doi.org/10.1016/j.polymertesting.2020.106965.
* Corresponding author.
E-mail address: patrick.gahlen@covestro.com (P. Gahlen).

https://doi.org/10.1016/j.polymertesting.2021.107234

Available online 23 May 2021

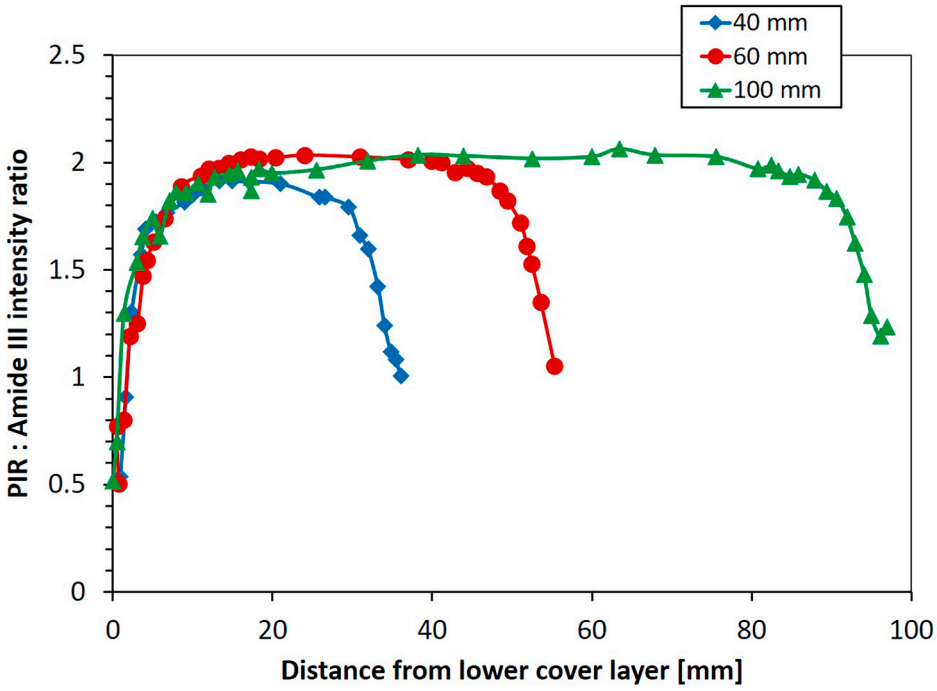
40 mm
60 mm
100 mm
PIR : Amide III intensity ratio
Distance from lower cover layer [mm]
0
0.5
1
1.5
2
2.5
0
20
40
60
80
100

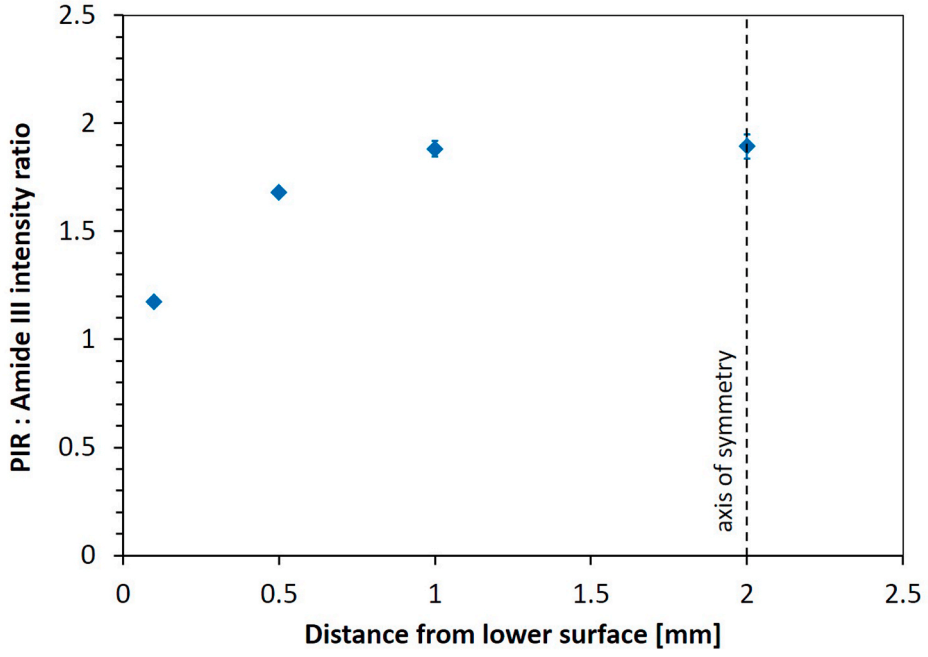
PIR : Amide III intensity ratio
Distance from lower surface [mm]
axis of symmetry
0
0.5
1
1.5
2
2.5

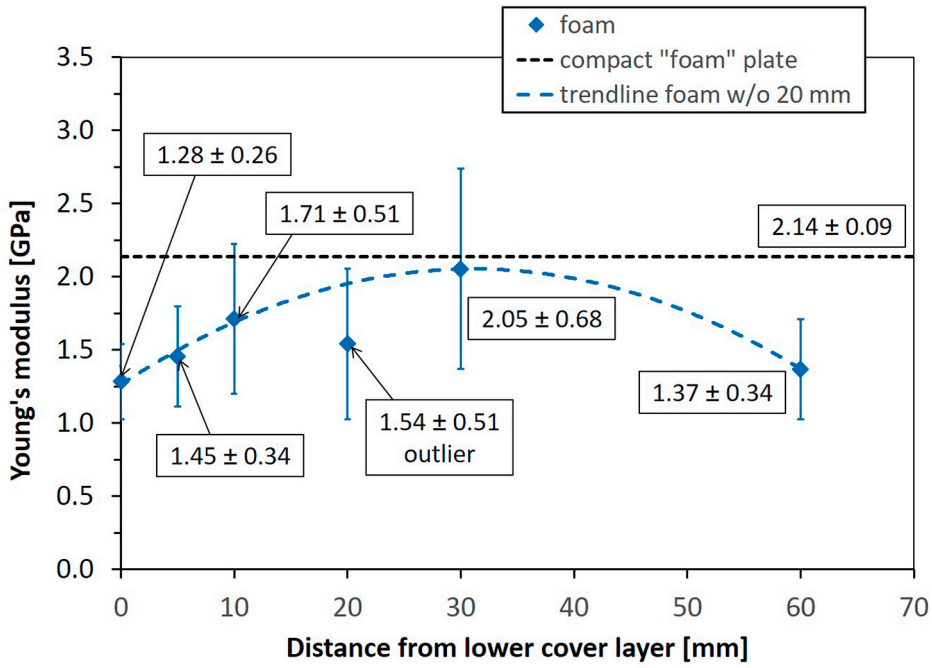
foam
compact "foam" plate
trendline foam w/o 20 mm
1.28 ± 0.26
1.71 ± 0.51
2.14 ± 0.09
2.05 ± 0.68
1.37 ± 0.34
1.54 ± 0.51
outlier
1.45 ± 0.34
Young's modulus [GPa]
Distance from lower cover layer [mm]
0.0
0.5
1.0
1.5
2.0
2.5
3.0
3.5
0
10
20
30
40
50
60
70

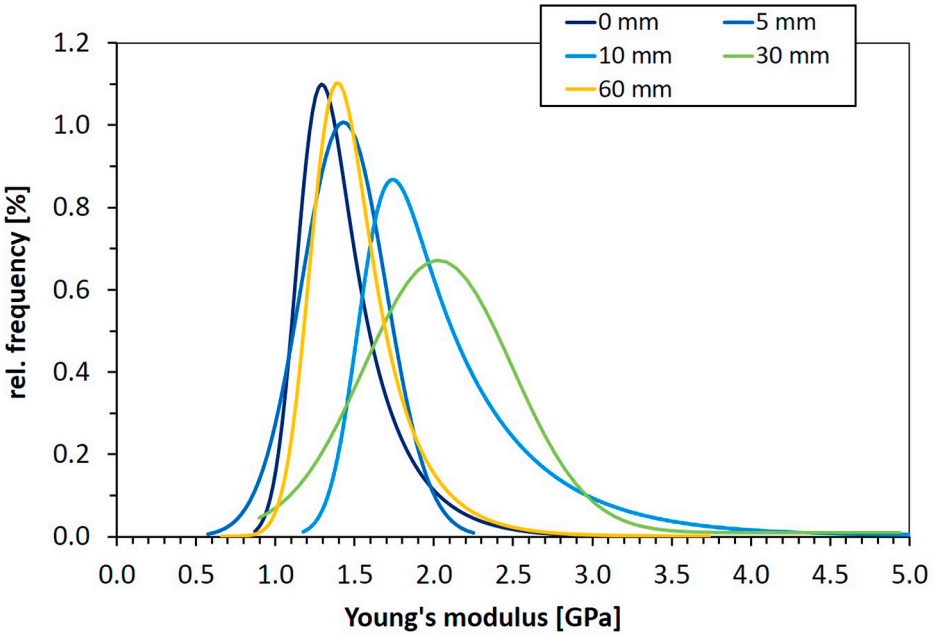
0 mm
5 mm
10 mm
30 mm
60 mm
rel. frequency [%]
Young's modulus [GPa]
0.0
0.2
0.4
0.6
0.8
1.0
1.2
0.0
0.5
1.0
1.5
2.0
2.5
3.0
3.5
4.0
4.5
5.0

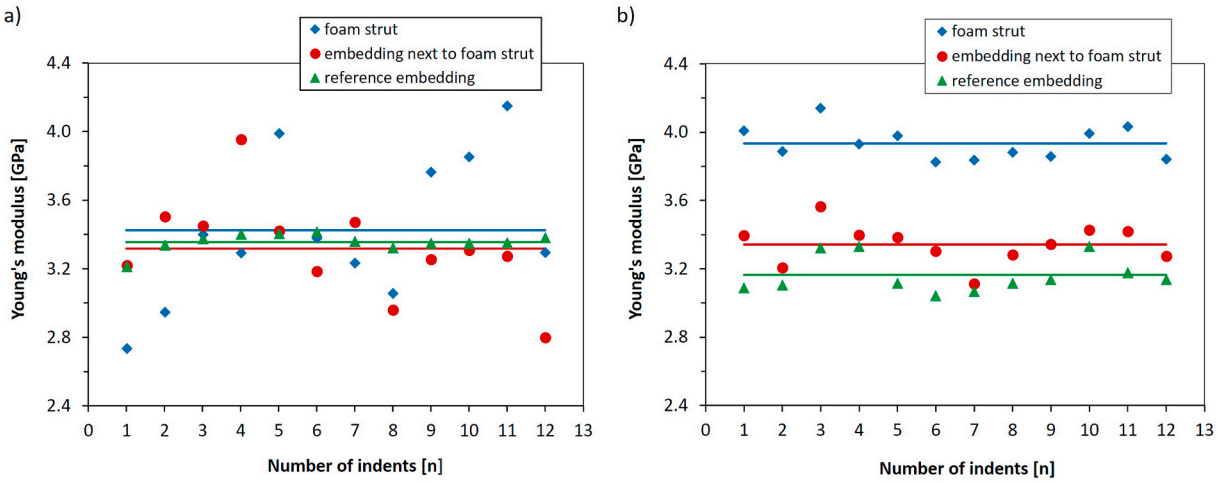
a)
b)
foam strut
embedding next to foam strut
reference embedding
Young's modulus [GPa]
Number of indents [n]

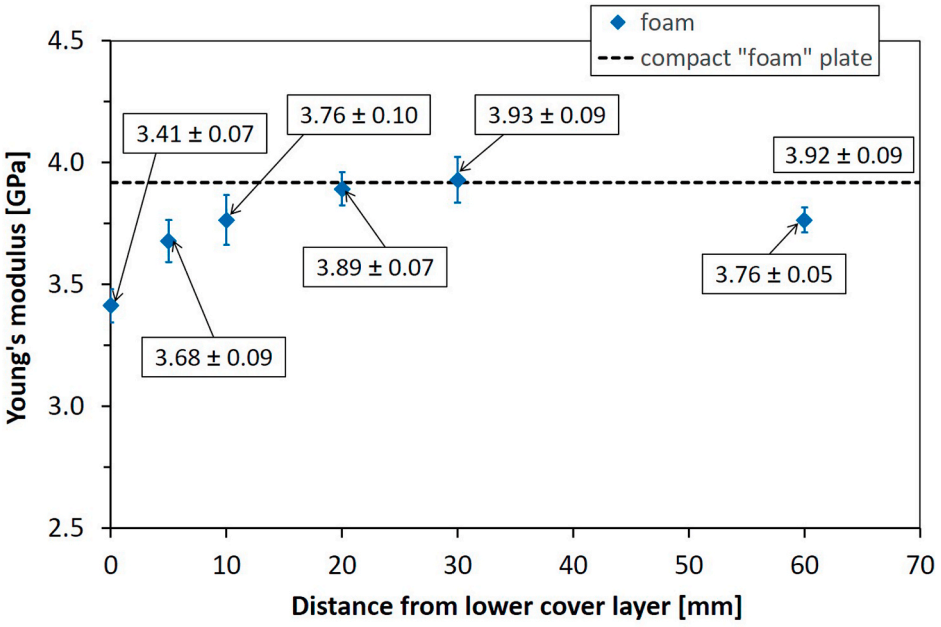
foam
compact "foam" plate
3.41 ± 0.07
3.76 ± 0.10
3.93 ± 0.09
3.92 ± 0.09
3.89 ± 0.07
3.76 ± 0.05
3.68 ± 0.09
Young's modulus [GPa]
Distance from lower cover layer [mm]

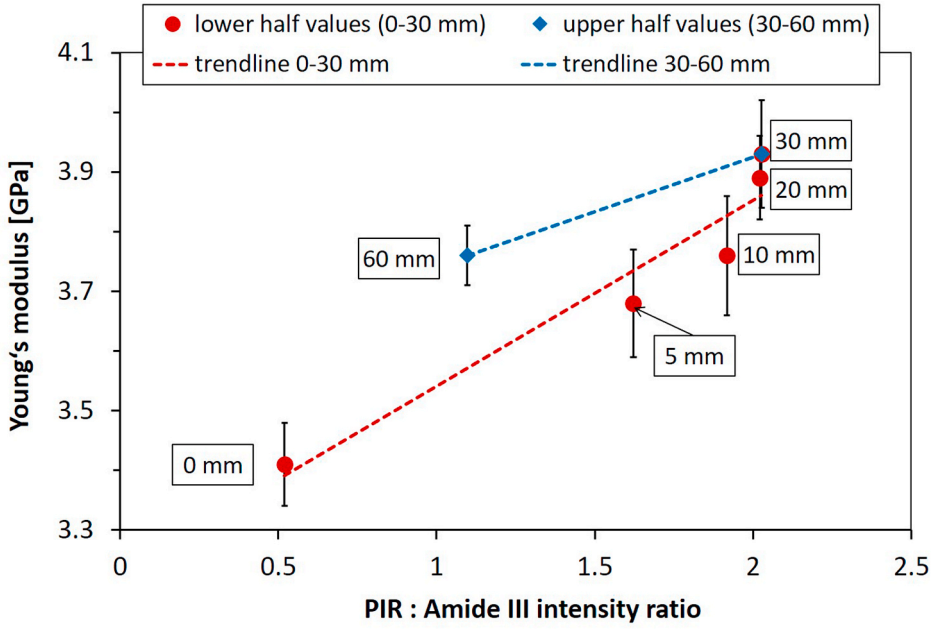
lower half values (0-30 mm)
upper half values (30-60 mm)
trendline 0-30 mm
trendline 30-60 mm
Young's modulus [GPa]
PIR : Amide III intensity ratio
4.1
3.9
3.7
3.5
3.3
0
0.5
1
1.5
2
2.5
0 mm
5 mm
10 mm
20 mm
30 mm
60 mm